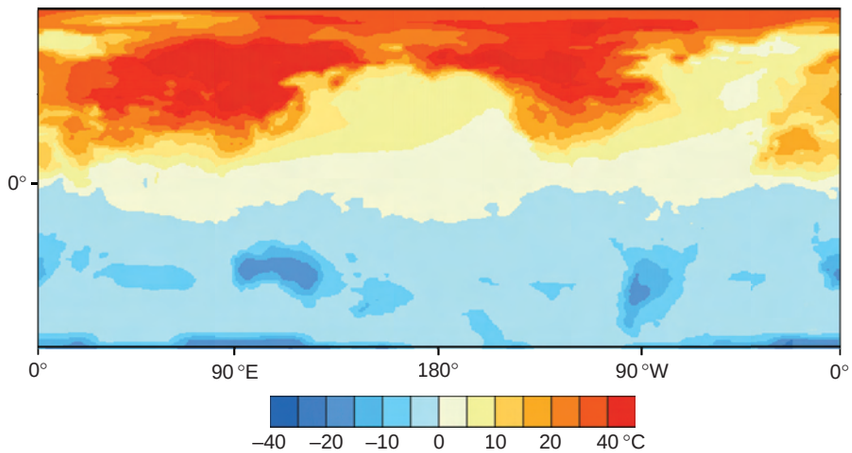

Fig. 10.8 The "Find the Continents" game! Climatological-mean July minus January surface air temperature in °C. [Courtesy of Todd P. Mitchell.]

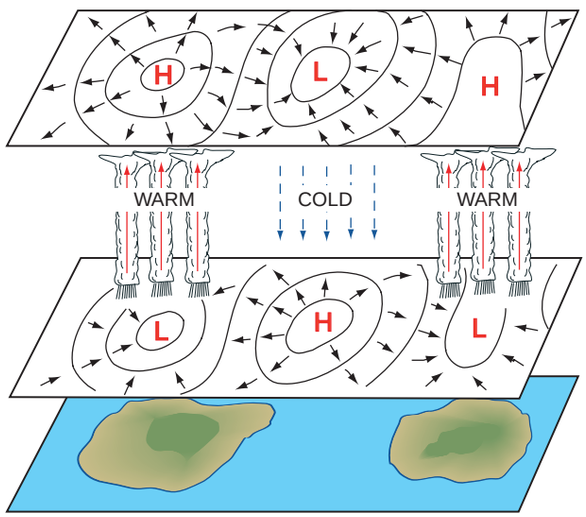

Fig. 10.9 Idealized representation of the monsoon circulations. The islands represent the subtropical continents in the summer hemisphere. Solid lines represent isobars or height contours near sea level (lower plane) and near 14 km or 150 hPa (upper plane). Short solid arrows indicate the sense of the cross-isobar flow. Vertical arrows indicate the sense of the vertical motions in the middle troposphere. Regions that experience of summer monsoon rainfall are also indicated.

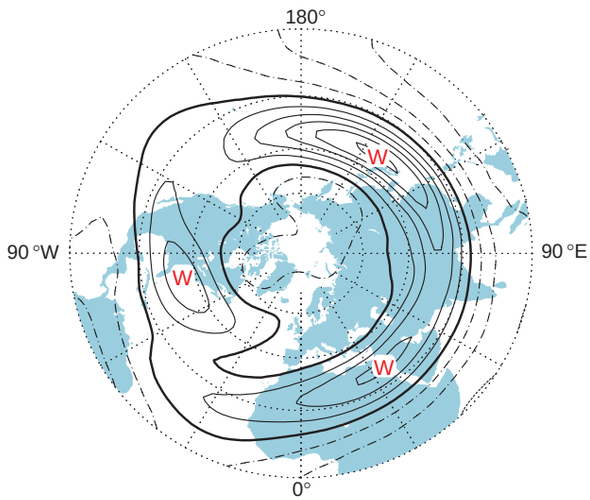

Fig. 10.10 January climatological mean zonal wind speed at the jet stream (250-hPa) level. Contour interval 15 m s^{-1}. The zero contour is bold; positive contours, indicative of westerlies, are solid and negative contours, indicative of easterlies, are dashed. [Based on data from the NCEP-NCAR Reanalysis. Courtesy of Todd P. Mitchell.]

tropospheric jet stream, the climatological mean westerly wind component at the 250-hPa level exceeds 70 m s^{-1} (Fig. 10.10). The Aleutian and Icelandic lows in the sea-level pressure field (Fig. 1.19) also tend to be most pronounced during wintertime, when the high latitude oceans are much warmer than the continents. In contrast, subtropical anticyclones tend to be strongest during summer, when they are reinforced by the monsoon-related land–sea pressure contrasts.

10.2 Climate Variability

Much of what we know about the causes of year-to-year climate variability is based on numerical experiments with atmospheric models like those described in Section 7.3. Imagine a pair of experiments: one run in which the bottom boundary conditions (e.g., sea-surface temperature, sea ice extent, soil moisture) are prescribed to vary from one year to the next in

accordance with historical data over, say, the 20th century and the other a run of equal length in which these boundary conditions are prescribed to vary in accordance with seasonally varying, climatological-mean values, year after year. Because weather is inherently unpredictable beyond a time frame of a few weeks, any resemblance between the observed and simulated 100-year sequence daily synoptic charts in the two simulations must be viewed as entirely fortuitous. However, the first run may exhibit climate variability attributable to the year-to-year variations in the boundary conditions, whereas the variability in the second run is generated exclusively by dynamical processes operating within the atmosphere. The ratio of the standard deviation of the year-to-year variability as simulated in the two experiments provides a measure of the relative importance of the *boundary forced* variability relative to the *internally generated* variability.

Numerical experiments of this kind have been conducted using many different models. The results can be summarized as follows.

(1) Most of the year-to-year variability of the tropical atmosphere is boundary forced (i.e., attributable to year-to-year variations in the prescribed boundary conditions, particularly sea-surface temperature over the tropical oceans). In the more realistic models, the simulated year-to-year variations in tropical climate bear a strong resemblance to the observed variations.

(2) At extratropical latitudes boundary forcing and internal atmospheric dynamics both make important contributions to the observed year-to-year climate variability. Of the various contributors to the boundary forcing, tropical sea-surface temperature appears to be of primary importance for the northern hemisphere winter climate. Variations in soil moisture and vegetation contribute to the month-to-month persistence of summertime climate anomalies. If the observed values of these fields are prescribed, the simulated year-to-year variations in extratropical climate are correlated with the observed variations, but not as strongly as in (1).

(3) The influences of year-to-year variations in sea-ice extent and extratropical sea-surface temperature are more subtle. By running ensembles of simulations, in which each member is started from different initial conditions but is forced with the same prescribed sequence of boundary conditions, it is possible to identify weak bondary-forced "signals" that stand out above the internally generated "sampling noise."

(4) Most of the intraseasonal variability of the extratropical wintertime circulation appears to be generated internally within the atmosphere.

Variability generated by the interactions between the atmosphere and more slowly varying components of the Earth system is referred to as *coupled climate variability*. Climate variability may also be *externally forced*, e.g., by volcanic eruptions, variations in solar emission, or changes in atmospheric composition induced by human activities.

10.1 Some Basic Climate Statistics[6]

Consider the climatic variable x, which could represent monthly-, seasonal-, annual-, or even decadal-mean temperature at a prescribed latitude, longitude, and height above the Earth's surface. Let X be the climatological-mean value of x. The departure of x from its (seasonally varying) climatological mean value, namely

$$x' = x - X \tag{10.1}$$

is referred to as the *anomaly* in x. For example, a temperature 3 °C below normal is equivalent to a temperature anomaly of −3 °C.

The *variance* of x about the climatological mean[7] is

$$\overline{x'^2} = \overline{(x - X)'^2} \tag{10.2}$$

where the $\overline{(\ )}$ denotes a time mean over the reference period upon which the climatology is based.

Continued on next page

[6] The formalism developed in Box 10.1 is also applicable to boundary-layer quantities. The overbars represent time-averaged quantities and the primed quantities represent fluctuations about the mean that occur in association with boundary-layer turbulence.

[7] $\overline{x'^2}$ is the *temporal variance*. The *spatial variance*, defined in an analogous manner, is a measure of the variability of x about its spatial mean.

10.1 Continued

Variance, a positive definite quantity with units of the square of the variable under examination (e.g., $°C^2$ for temperature), is a measure of the amplitude of the variability (or dispersion) of x about its climatological-mean value. The *standard deviation* or *root mean squared (r.m.s.) amplitude* of the variations in x about the time mean

$$\sigma(x) \equiv \sqrt{x'^2} = \sqrt{(x - X)'^2} \qquad (10.3)$$

is widely used as a measure of the dispersion. Note that variance and standard deviation do not carry algebraic signs.

The *standardized anomaly*

$$x^* \equiv \frac{x'}{\sigma(x)}$$

is a dimensionless measure of the amplitude of the departure from the mean. For variables such as monthly-mean temperature, sea-level pressure and geopotential height, which tend to be *normally distributed*,[8] ~64% of randomly selected standardized anomalies exhibit absolute values less than 1.0, ~95% of them less than 2.0, and ~99.9% of them less than 3.0. Hence, for such distributions, a standardized anomaly x^* with a value of +1.0 or −1.0 can be considered typical in terms of r.m.s. amplitude.

Figure 10.11 shows an example of a seasonal mean 500-hPa height field together with the corresponding anomaly and standardized anomaly fields. In contrast to the baroclinic waves discussed in Section 8.1.1, which exhibit typical zonal wavelengths of ~40° of longitude, the anomalies in monthly and seasonal mean fields like the ones shown in this example are larger in scale and they are not particularly wave like.

Now let us consider the relationship between two time series $x(t)$ and $y(t)$, which might represent a series of values of the same climatic variable at two different geographical locations or might represent two different variables at the same location. It is assumed that $x(t)$ and $y(t)$ span a common period of record. The dimensionless statistic

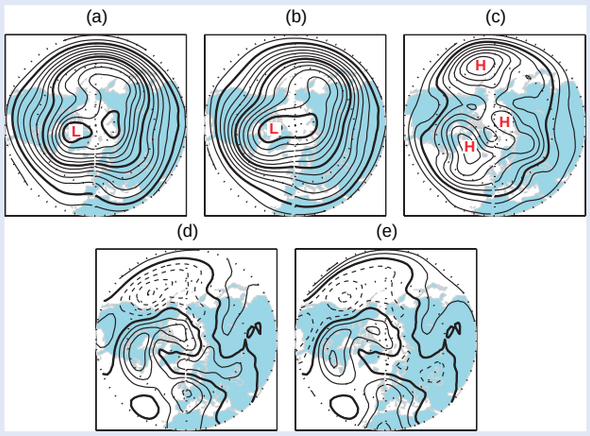

Fig. 10.11 (a) The mean 500-hPa height field averaged over the late winter season January–March 1998. (b) The climatological-mean wintertime (January–March) 500-hPa height field based on the period of record 1958–1999; contour interval 60 m, the 5100-, 5400- and 5700-m contours are bold. (c) The climatological-mean standard deviation of the wintertime-mean (January–March) 500-hPa height field based on the same period of record; contour interval 9 m, the 54-m contour is bold. (d) The anomaly field for January–March 1998, calculated by subtracting (b) from (a); contour interval 30 m, the zero contour is bold, and dashed contours denote negative values. (e) The standardized anomaly field, calculated by dividing (d) by (c); contour interval 0.6 standard deviations, the zero contour is bold, and dashed contours denote negative values. [Based on data from the NCEP-NCAR Reanalyses. Courtesy of Roberta Quadrelli.]

Continued on next page

[8] Possessing a bell-shaped histogram centered on the climatological-mean value, with a width (defined as the distance between the center and the inflection points) of 1 standard deviation.

10.1 Continued

$$r \equiv \overline{x^* y^*} \equiv \frac{\overline{x' y'}}{\sigma(x)\,\sigma(y)} \qquad (10.4)$$

called the *correlation coefficient* between x and y, is a measure of the degree to which x and y are *linearly* related (i.e., that one is simply a linear multiple of the other). Values of r range from -1 to $+1$.

To illustrate how the correlation coefficient can be used to describe the structure of a spatial field, we show, in Fig. 10.12, scatter plots of standardized wintertime mean sea-level pressure anomalies over Iceland versus sea-level pressure at three different locations. In plot A, y Iceland sea-level pressure is plotted against sea-level pressure at a nearby location; in this case x^* and y^* tend to be of like sign so that $r = \overline{x^* y^*} > 0$ and the data points in the scatter plot lie preferentially in the first and third quadrants of the plot. In such situations x and y are said to be *positively correlated*. Plot B shows pressure over Iceland versus sea-level pressure over southern England; in this case the correlation is weak (i.e., $r \sim 0$). Plot C shows that sea-level pressure anomalies over Iceland and Portugal tend to be of opposing sign (i.e., negatively correlated: $r = \overline{x^* y^*} < 0$ and the points in the plot lie preferentially in the second and fourth quadrants. Statistically significant linear correlations between climatic variables such widely spaced locations are evidence of what are referred to as *teleconnections*.

In general, the higher the value of $|r|$, the tighter the clustering of the dots along the 45° (or 135°) axis in scatter plots of x^* versus y^*. It can be shown that in the limit, as $|r| \to 1$, the points line up perfectly, in which case, $y^* = rx^*$ or, alternatively, $x^* = ry^*$. If $r = 0$, there is no linear relation between x and y and the least-squares best fit in the scatter plot is the horizontal line that passes through the centroid of the data points. Exercise 10.9 shows that the fraction of the variance of x and y that is common to the two variables (in a linear sense) is given by r^2.[9]

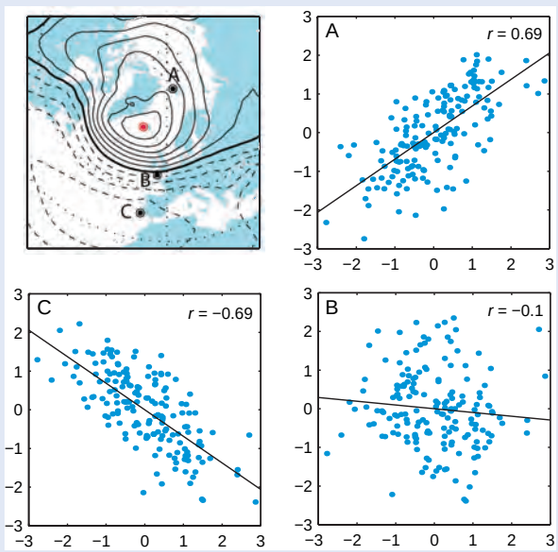

Fig. 10.12 Scatter plots of standardized sea-level pressure anomalies. In all three plots, the x axis refers to anomalies at a grid point over Iceland, indicated by the red dot in the upper left panel. Iceland anomalies are plotted versus anomalies at (**A**) Spitzbergen, (**B**) southern England, and (**C**) Portugal. Numerical values of the correlation coefficients are indicated in the scatter plots, and sloping lines represent the equation $y^* = rx^*$ that corresponds to the least-squares best fit linear regression line. The map in the upper left panel shows the correlation coefficient between sea-level pressure at Iceland and sea-level pressure at every grid point: contour interval 0.15; the zero contour is bold and negative values are indicated by dashed contours. [Based on data from the NCEP-NCAR Reanalyses. Courtesy of Roberta Quadrelli.]

[9] The correlation coefficient r can also be interpreted as the slope of the *least-squares best fit regression line* for y regressed upon x; i.e., the slope of the staight line, passing through the origin, for which the mean squared error $(y_i - rx_i)^2$, summed over all data points in the time series, is minimized (see Exercise 10.9).

10.2.1 Internally Generated Climate Variability

The day-to-day variability of the geopotential height field is characterized by a bewildering array of hemispheric patterns. In contrast, the spatial patterns of month-to-month variability, as manifested in hemispheric or global anomaly fields like those shown in Fig. 10.11 tend to be simpler. Much of the structure in such maps can be interpreted in terms of the superposition of a limited number of *preferred spatial patterns* that may appear with either polarity when they are present. In the northern hemisphere these patterns are much more prominent during winter than during summer.

A prominent pattern in the northern hemisphere wintertime geopotential height field is variously known as the *North Atlantic Oscillation (NAO)*, the *Arctic Oscillation (AO)*, or the *northern hemisphere annular mode (NAM)*. The sea-level pressure signature of this pattern, shown in Fig. 10.13, is marked by anomalies of opposing sign over the Arctic polar cap region and the Atlantic/Mediterranean sector of middle latitudes. The Southern hemisphere annular mode (not shown) is even more symmetric about the pole and is evident not just during the winter, but throughout the year.

When sea-level pressure is below normal over the polar cap region and above normal over the Mediterranean, the annular mode is said to be in its *high index* polarity. At these times the jet streams and storm tracks tend to be displaced poleward of their normal positions, temperatures tend to be unseasonably mild over Eurasia and most the United States (Fig. 10.14), and northern Europe experiences

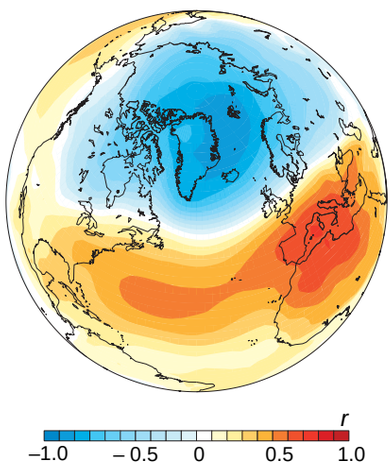

Fig. 10.13 Pattern of sea-level pressure anomalies associated with the *northern hemisphere annular mode* (a.k.a., *North Atlantic Oscillation*). Colored shading indicates the correlation coefficient between the time series of the index of the pattern shown in Fig. 10.17 and the time series of the monthly mean sea-level pressure anomalies at each grid point. The colors thus indicate the sign of the anomalies associated with the high index polarity of the annular mode: the low index polarity is characterized by anomalies of opposite sign. [Based on November–April data from the NCEP-NCAR Reanalysis. Courtesy of Todd P. Mitchell.]

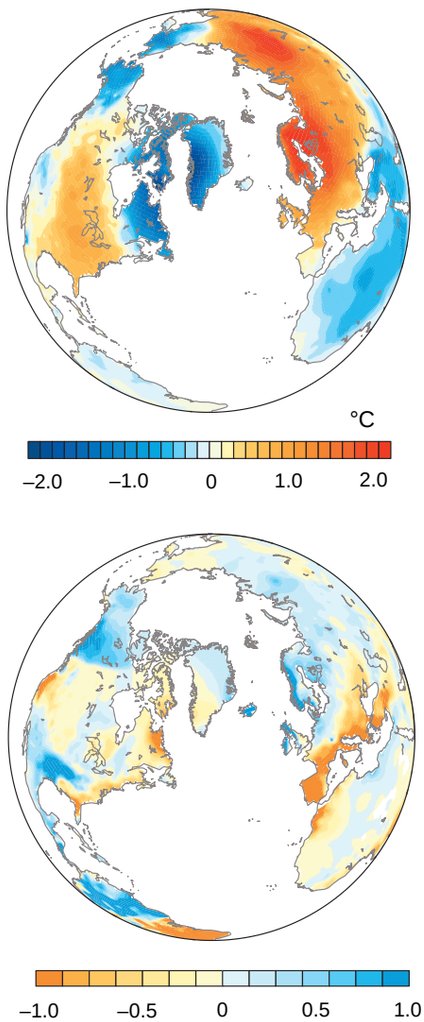

Fig. 10.14 Patterns of surface air temperature anomalies (top) and standardized precipitation anomalies (bottom) observed in months when the northern annular mode is in its *high index polarity* characterized by below normal sea-level pressure over the Arctic. Warm colors indicate above normal temperature and below normal precipitation, and shades of blue indicate anomalies of opposing sign. Typical amplitudes of the temperature and standardized precipitation anomalies are indicated by the color scale. [Courtesy of Todd P. Mitchell.]

heavier than normal rainfall while the Mediterranean basks in sunshine. In contrast, episodes of abnormally high pressure over the Arctic (i.e., the *low index polarity* of the annular mode) tend to be marked by relatively frequent occurrence of cold-air outbreaks over Eurasia and the United States, raising the demand for heating oil on the world market, and stormy weather over the Mediterranean.

The sea-level pressure signature of another prominent wintertime pattern, the so-called *Pacific/North American (PNA) pattern*, is shown in Fig. 10.15. The PNA pattern, with its strongest sea-level pressure anomalies over the North Pacific, has a strong impact on wintertime climate anomalies downstream over North America, as documented in Fig. 10.15. When pressures over the North Pacific are below normal, temperatures over much of western North America tend to be relatively mild and precipitation tends to be abnormally heavy along the coasts of the Gulf of Alaska and the Gulf of Mexico; Hawaii tends to be dry.

The processes that give rise to the annular modes and PNA pattern are not fully understood. The annular modes involve north–south shifts in the *storm tracks* (i.e., the belts of strongest baroclinic wave activity) and the surface westerlies. When the annular modes are in their high index polarity, the storm tracks and associated westerly wind belts are shifted poleward of their climatological-mean positions, and vice versa. These shifts are believed to occur as a result of the interactions between the waves and the mean westerly winds upon which they are superimposed. The PNA pattern, which has no clearly defined southern hemisphere counterpart, involves the alternating extension and retraction of the downstream end of the jet stream that passes just to the south of Japan in Fig. 10.10. When the PNA pattern is in its high index polarity, the jet extends farther east into the central Pacific than in Fig. 10.10, and vice versa. These extensions and retractions of the jet are believed to be the manifestation of a form of instability of the northern hemisphere wintertime climatological-mean stationary-wave pattern.

The annular modes and the PNA pattern play important roles in the variability of the extratropical circulation on timescales of decades and longer. Of particular interest is the tendency toward the positive polarity of both northern and southern annular modes from the 1970s to the 1990s (Fig. 10.17). The positive trends in the indices of the annular modes

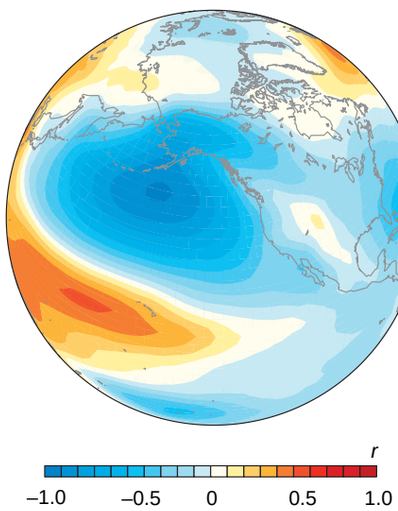

Fig. 10.15 As in Fig. 10.13, but for the Pacific/North American pattern. [Courtesy of Todd P. Mitchell.]

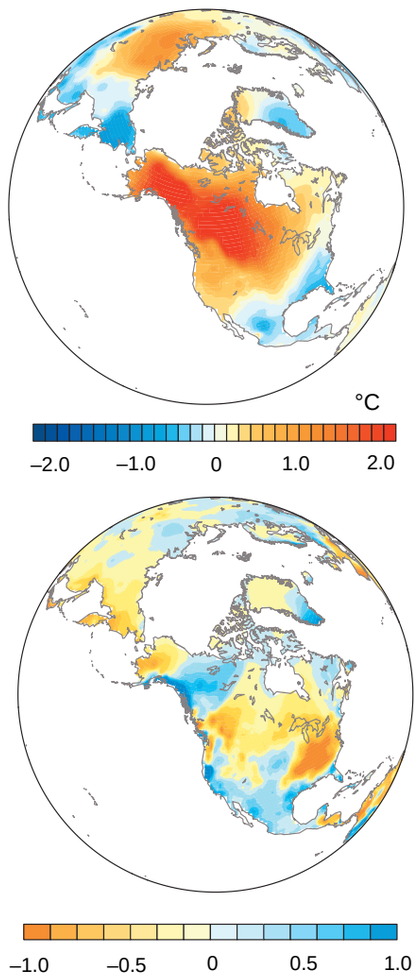

Fig. 10.16 As in Fig. 10.14, but for the Pacific/North American pattern. [Courtesy of Todd P. Mitchell.]